Photo-induced processes for the fabrication of nanocomposite PEO/GO electrospun nanofibers with enhanced thermal conductivity

Photo-induced processes for the fabrication of nanocomposite PEO/GO electrospun nanofibers with enhanced thermal conductivity

Parnian Kianfar[1] ● Sara Dalle Vacche[1,2] ● Giulia Fredi[3] ● Roberta Bongiovanni[1,2] ● Alessandra Vitale[1,2]

Received: ……/Accepted …

Abstract A simple, rapid, and environmentally friendly strategy for fabricating shape-stable, thermally conductive nanocomposite fibers based on poly(ethylene oxide) (PEO) and graphene oxide (GO) is reported. The method integrates electrospinning with UV-induced photocrosslinking and *in situ* photoreduction, simultaneously enhancing the insolubility of PEO fibers and restoring the thermal conductivity of GO. Cast film studies confirmed the partial reduction of GO upon UV irradiation in the presence of a photoinitiator, contributing to improved thermal transport. A Taguchi Design of Experiments (DoE) approach was employed to optimize the fabrication of electrospun mats. The resulting nanocomposite membranes exhibited excellent shape stability under heat and solvent exposure, preserved fiber morphology, and showed enhanced thermal diffusivity across a range of temperatures.

Keywords Graphene oxide ● Electrospinning ● Photochemistry ● Nanostructures ● Reductions

✉ Alessandra Vitale
alessandra.vitale@polito.it

[1] Department of Applied Science and Technology, Politecnico di Torino, 10125 Torino, Italy

[2] INSTM – Politecnico di Torino Research Unit, 50121 Firenze, Italy

[3] Department of Industrial Engineering, University of Trento, 38123 Trento, Italy

Introduction

Electrospinning is an attractive technique for producing fibrous mats with fiber diameters ranging from a few nanometers to micrometers. These fibrous materials are characterized by a high surface-to-volume ratio, morphological and compositional versatility, tunable porous structure, and the ability to conform to various shapes and sizes [1-3]. The method is also valued for its simplicity, scalability, high productivity, and reproducibility. It has been used to process a wide range of polymers, both from solutions and melts [4]; even latexes and prepolymers can be successfully electrospun [5]. Moreover, electrospun fibrous nanocomposites can be easily fabricated, offering advantages such as preventing nanoparticle agglomeration and enabling uniform nanofiller distribution. Incorporation of nanofillers into polymeric nanofibers enhances their physical and mechanical properties while also imparting specific functionalities [6-8]. Consequently, electrospun nanocomposites have found applications across diverse fields, including biomedicine [9,10], sensing [11], water treatment [12], and energy devices [13].

A wide range of polymers has been utilized as the organic phase in electrospun nanocomposites to tailor the properties and functionalities of the fibrous matrix. In this study, poly(ethylene oxide) (PEO) was selected due to its abundance and exceptional properties, including biocompatibility,

chemical inertness, high thermal stability, and excellent electrospinnability, in addition to good electrochemical stability and the ability to dissolve a variety of salts. However, one of the major limitations of PEO-based membranes is their high solubility in water and many common organic solvents. We have recently demonstrated that this limitation can be effectively addressed by photocrosslinking the electrospun PEO materials, resulting in the formation of a stable covalent network [14-18]. Moreover, neat PEO films and nanofibers are generally thermally insulating, which restricts their application in energy-related fields, e.g., for thermal energy storage, as discussed in previous work [17]. Enhancing their thermal conductivity can thus significantly expand their utility. This can be achieved by incorporating graphene and its derivatives.

Graphene, a two-dimensional sheet of sp^2-hybridized carbon atoms arranged in a honeycomb lattice, exhibits exceptional thermal (~3000 W/(m·K)) and electrical conductivity, along with a high aspect ratio, excellent topographical features, large specific surface area, and outstanding mechanical properties. Owing to these superior characteristics, graphene-based materials are widely recognized as promising candidates for the development of polymer nanocomposites, offering significant enhancements in mechanical, electrical, and thermal performance [19,20]. However, despite these advantages, graphene is not easily dispersible, particularly in

polar polymers such as PEO. To address this limitation, its oxidized form (graphene oxide, GO) is often employed. GO contains various oxygenated functional groups (e.g., hydroxyl, epoxide, and carboxyl) on its basal planes, which impart hydrophilicity and enable good dispersibility in aqueous media, thus facilitating processing. However, the introduction of sp^3-hybridized carbons disrupts the sp^2 network, rendering GO electrically insulating [21]. To restore its electrical conductivity, GO must undergo a reduction process to partially or fully recover the conjugated graphene structure. Various reduction strategies have been employed, including chemical and electrochemical methods, which are among the most widely used [22-24]. Photo-irradiation, particularly UV treatment, has also proven effective in reducing GO [25]. During this process, the oxygen-containing functional groups are reduced while the underlying graphene carbon skeleton is preserved, owing to its greater stability compared to the oxygenated moieties [26]. This approach often involves the use of a photoinitiator or catalyst to enhance the reaction: they easily produce free radicals, which are well-known powerful reducing agents. In particular, photoinitiators with very short triplet lifetimes promote the rapid formation of photoreduced GO [27].

UV-assisted reduction offers several advantages such as simplicity, cleanliness, and low cost. Notably, the photo-induced reduction of GO can

be carried out *in situ*, simultaneously with the photopolymerization or photocrosslinking of the polymer matrix [28-31].

In this study, we present a simple, rapid, and environmentally friendly strategy to fabricate thermally conductive nanocomposite fibers based on PEO and GO. This approach combines electrospinning with photo-induced reactions to simultaneously achieve insolubility of the electrospun PEO through photocrosslinking and enhanced thermal properties through photoreduction of GO. Electrospun nanocomposites incorporating GO or reduced GO have been widely investigated in the literature for various applications, including biomedicine e.g., wound healing [32,33], tissue engineering [34,35], and drug delivery [36], electronics [37], energy devices [38,39], sensors [40,41], water treatment filters [42], and packaging materials [43]. These studies highlight the broad application potential of the materials and processing strategy developed in this work.

Results and Discussion

Electrospun nanocomposite membranes incorporating GO were fabricated from PEO solutions containing a photocrosslinker (trimethylolpropane trimethacrylate, TMPTMA) and a photoinitiator (benzophenone, PI). Subsequent UV irradiation promoted two simultaneous processes: (i) the radical-mediated crosslinking of the polymer network, driven by the

reactivity of the acrylic groups in TMPTMA and the hydrogen abstraction from the PEO main chain [16], and (ii) the *in situ* photochemical reduction of GO. This dual mechanism results in water insoluble, shape-stable nanofibrous membranes with embedded reduced GO, as schematized in Figure 1.

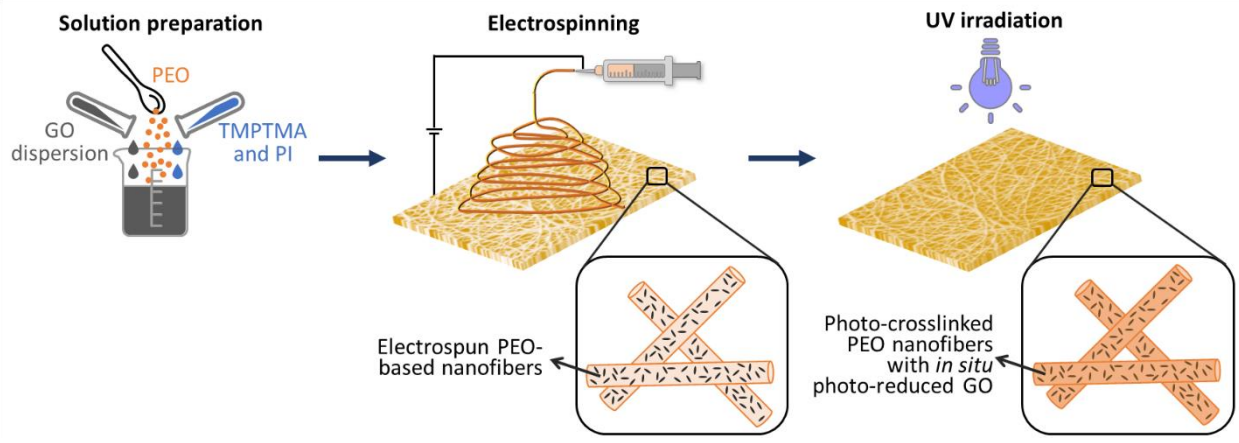

Fig. 1 Schematic illustration of the photo-induced fabrication of crosslinked PEO-based electrospun nanofibers incorporating *in situ* reduced GO

Photo-induced reduction of GO

To preliminarily investigate the photo-induced reduction of GO, an aqueous dispersion of GO containing benzophenone as photoinitiator was irradiated with UV light. The photoreduction process was monitored using UV-Vis spectroscopy by recording spectra before and after irradiation (Figure 2). Prior to irradiation, the spectrum exhibited a strong absorption peak from the photoinitiator centered at 257 nm, along with a shoulder peak around 200

nm corresponding to GO. After irradiation, the characteristic GO peak disappeared, and the main peak shifted to 250 nm. This shift indicates both the consumption of the photoinitiator and the partial restoration of the π-conjugated network, accompanied by the aggregation of reduced GO [27].

These spectral results were supported by visual observations of the GO dispersion before and after irradiation. Initially, the dispersion appeared homogeneous and relatively clear, which is consistent with the high dispersibility of GO in water due to its oxygen-rich functional groups. However, upon reduction, the removal of these groups renders GO less dispersible in water. Following UV exposure, the dispersion became more heterogeneous, and dark brownish particles were clearly visible, indicating aggregation of the reduced GO [27] (as shown in the insets of Figure 2).

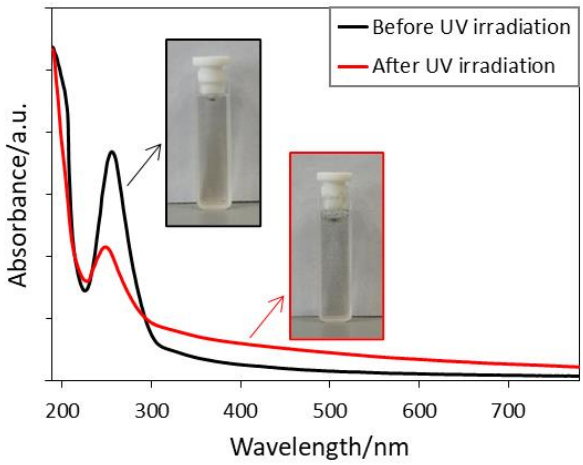

Fig. 2 UV-Vis spectra and photographs of GO water dispersion in the presence of the photoinitiator, before and after irradiation

To confirm and further investigate the photoinduced reduction of GO even within a polymer matrix, cast PEO films were prepared and analyzed using Fourier Transform Infrared spectroscopy in attenuated total reflectance mode (FTIR-ATR) and X-ray diffraction (XRD). A model system containing 25 wt.% of the crosslinker TMPTMA (XL) and 1 wt.% GO was irradiated with UV light and characterized before and after irradiation.

FTIR spectroscopy, although commonly used to monitor GO reduction via the attenuation of the bands associated with oxygenated groups (e.g., hydroxyl, epoxide, carboxyl), was not effective in this case. In fact, the characteristic GO peaks overlapped with strong signals from PEO and TMPTMA, and no discernible differences were observed between spectra of films with and without GO. FTIR-ATR measurements taken on both sides of the films were useful to monitor the crosslinking reaction: as expected, after irradiation, the decrease of the peak at 1638 cm^{-1} related to the C=C reactive groups of the crosslinker is evident (Supporting Information, Figure S1), suggesting the occurrence of the photocrosslinking reaction with a conversion around 40% [17]. Moreover, no significant differences were detected between the front side (i.e., top surface) and the back side (i.e., bottom surface) of the samples (Figure S2 in the Supporting Information).

XRD analysis provided more detailed insights into the expected photoreduction process. As shown in Figure 3a, films containing 1 wt.% GO

did not exhibit the characteristic GO (002) diffraction peak at $2\theta \approx 12°$, which corresponds to the average interlayer spacing of graphene oxide, nor the (10) diffraction peak at $2\theta \approx 42°$, indicative of short-range ordering in stacked graphene layers. Instead, the spectrum displayed features attributable to PEO [44]: as visible in the XRD of the powder, PEO has a monoclinic crystalline structure, with the (120) planes aligned parallel to the chain direction and the (112) planes intersecting it, which produce strong diffraction peaks at $2\theta \approx 19°$ and 23°, respectively. The observed shift in the nanocomposite films diffraction positions and the reduction in the intensity of PEO characteristic peaks, along with the absence of the GO (10) peak, suggest that PEO may interact with GO via hydrogen bonding, leading to an exfoliated structure [45]. After UV exposure, no new diffraction peaks appeared, as expected: the (002) peak of reduced GO typically shifts to around $2\theta \approx 24°$, overlapping with the PEO peaks, making it difficult to resolve. Furthermore, the continued absence of the (10) peak near $2\theta \approx 43°$, similar to that of pristine GO, supports the absence of stacked GO layers although non demonstrating their reduction. To enhance detection sensitivity, a film containing 5 wt.% GO was also analyzed (Figure 3b). In this case, the GO (002) peak at $2\theta \approx 12°$ was clearly visible before irradiation, indicating that at higher concentrations, intercalation with PEO was incomplete. Interestingly, after UV treatment, the intensity of this peak

significantly decreased. This observation, consistent with literature [46], qualitatively confirms the successful photo-induced reduction of GO within the photocrosslinked polymer matrix. Additionally, the broad signal and few emerging peaks in the *2θ* range of 19°–24° can be attributed to both reduced GO and PEO. The broadening of these peaks is likely due to a reduction in crystallite size, changes in interlayer spacing, and the development of an amorphous phase in the polymer matrix, promoted by the presence of graphene nanosheets.

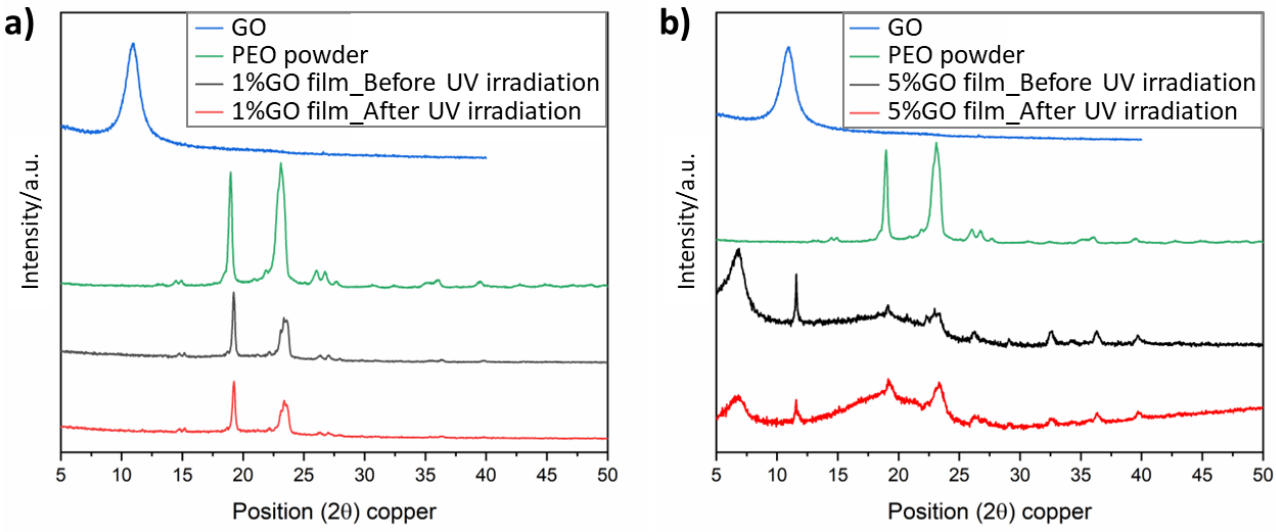

Fig. 3 XRD patterns of GO, PEO powder and PEO/XL/GO cast films with 1 (a) and 5 wt.% (b) GO, before and after UV irradiation

The thermal diffusivity of cast films was evaluated to assess the impact of GO addition and UV irradiation. In particular, the system containing 25 wt.% XL and 1 wt.% GO was characterized before and after

UV irradiation. Moreover, an irradiated film without GO was used as reference. As shown in Figure 4, the diffusivity of any sample generally decreased with increasing temperature, consistent with expectations. Notably, films containing GO, prior to photo-induced reduction, showed similar thermal diffusivity to neat PEO/XL films. In fact, the oxygenated functional groups on GO introduce structural imperfections, significantly disrupting phonon transport. Irradiated GO-containing films had instead higher thermal diffusivity over the investigated temperature range (Figure 4). These results indicate that upon UV irradiation GO is partially reduced with restoration of sp^2 carbon networks, leading to enhanced phonon transport and improved thermal diffusivity. Indeed, the degree of this enhancement depends on the extent of reduction and the presence of residual structural defects. It is therefore reasonable to expect that thermal diffusivity may increase with increasing irradiation, up to a certain point.

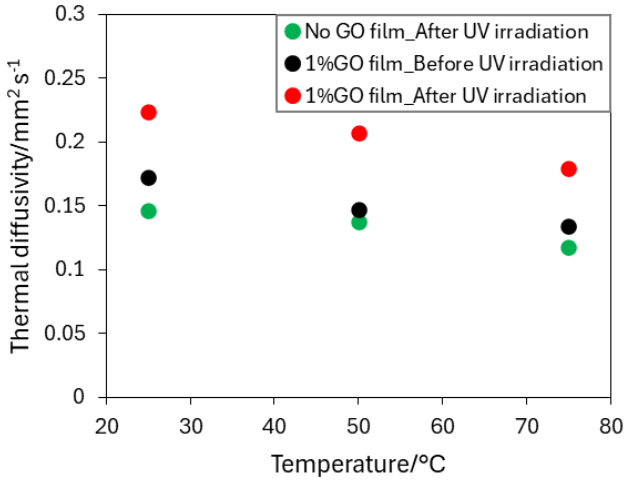

Fig. 4 Thermal diffusivity of PEO/XL/GO cast films with 0 and 1 wt.% GO, before and after UV irradiation (with a UV dose of 42 J/cm^2)

Fabrication and optimization of PEO/GO photocured electrospun nanofibers

PEO-based electrospun membranes embedding GO were fabricated following the method depicted in Figure 1. As previously reported [16,17], PEO can be readily electrospun from solution; however, due to its polar and hydrophilic nature, the resulting fibers are water soluble. To optimize the production of shape-stable, thermally and chemically resistant electrospun nanocomposite mats, a Taguchi Design of Experiment (DoE) was implemented. This method, widely used in materials engineering, enables efficient data collection under controlled conditions and helps identify key controllable factors that minimize the impact of uncontrollable "noise" factors. By manipulating these noise factors during testing, Taguchi designs determine the optimal settings for a robust process performance. The use of orthogonal arrays allows for independent assessment of each factor, reducing experimental time and cost while maintaining statistical balance. In this study, three factors were evaluated at three levels each (see Experimental section): crosslinker (XL) content ranging from 6.25 to 25.00 wt.%, GO content between 0.5 and 2.0 wt.%, and UV dose (*d*, defined as the product of the light intensity and the irradiation time) from 21 to 84 J/cm^2. The

selected levels were based on our previous works [16,17], which showed that a system containing 25 wt.% crosslinker and irradiated with 84 J/cm² UV dose produced thermally resistant, shape-stable neat PEO electrospun mats. An L9 orthogonal array was employed to design the experiments, as summarized in Table 1.

Table 1. Taguchi L9 experimental orthogonal array design for electrospun nanocomposites

Exp. #	XL/wt.%	GO/wt.%	d/J cm^{-2}
1	6.25	0.5	21
2	12.5	1	21
3	25	2	21
4	6.25	1	42
5	12.5	2	42
6	25	0.5	42
7	6.25	2	84
8	12.5	0.5	84
9	25	1	84

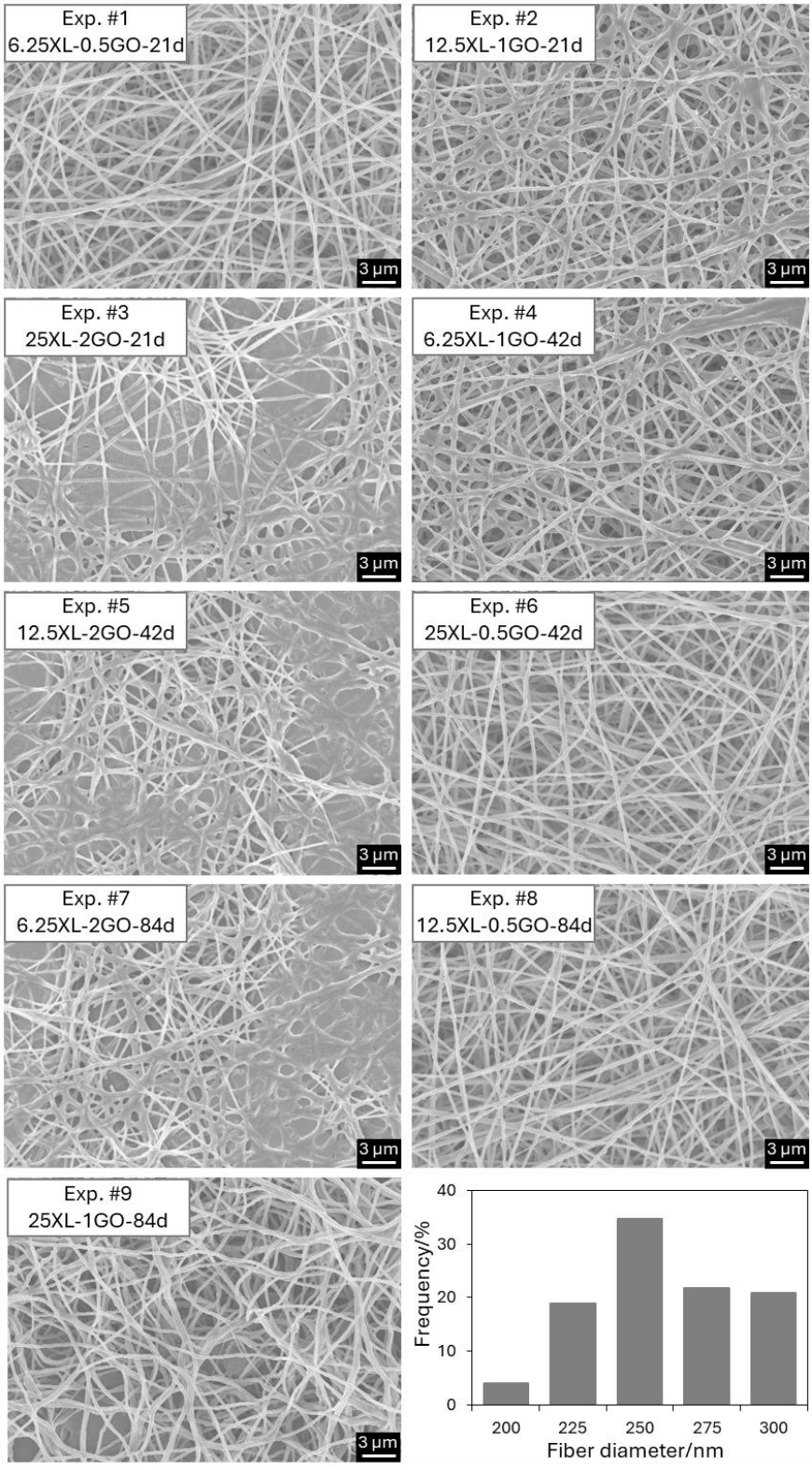

Fig. 5 Morphology of the nanocomposite PEO-based electrospun mats: FESEM images and fiber diameter distribution

Most formulations and process conditions yielded defect-free, photocrosslinked nanofibers (Figure 5). However, samples containing 2 wt.% GO (Exp. #3, #5, #7) exhibited agglomeration and fiber collapse upon UV exposure, resulting in non-uniform structures. In contrast, other formulations produced uniform, cylindrical fibers with average diameters of 247 ± 28 nm (Figure 5).

To assess shape stability towards chemicals and heating, two tests were conducted: (i) solvent resistance (immersion in distilled water for 24 h) and (ii) thermal resistance (heating at 100 °C, i.e., above PEO melting point of 62.2°C [17], for 30 min). Morphological integrity was qualitatively scored as 1 (stable), 0 (partially stable), or –1 (unstable), based on optical microscopy observations (Table 2). The results showed that most mats had better resistance to solvent than heat. Moreover, only sample #6 (25 wt.% XL, 0.5 wt.% GO, dose of 42 J/cm²) and sample #9 (25 wt.% XL, 1 wt.% GO, dose of 84 J/cm²) retained full structural integrity after both treatments.

Table 2. Shape stability results from solvent and thermal treatments of the L9 experiments: 1 = shape-stable, 0 = partially shape-stable, -1 = shape unstable

Exp. #	Shape stability response	
	Solvent resistance	Thermal resistance
1	-1	-1
2	1	0
3	1	0
4	-1	-1
5	0	0
6	1	1
7	-1	-1
8	0	0
9	1	1

To better understand the effects of each factor, the signal-to-noise (*S/N*) ratio was analyzed. The *S/N* ratio represents the relationship between the desired output (signal) and the undesired variation (noise), summarizing multiple data points within a single trial. In this study, a “larger is better” criterion was applied to maximize mat stability. The *S/N* ratios for the three investigated factors, based on two responses (i.e., solvent resistance and thermal resistance) are shown in Figure 6. A mean *S/N* value of 5.1 was identified as the threshold above which the mats are considered shape stable.

The results shown in Figure 6 confirmed that crosslinker content was the most influential parameter. A content above 12.5 wt.% was critical for stability (samples containing 6.25 wt.% XL were not resistant to either solvent or thermal treatments). Although the GO content had a minor overall effect, excessive loading (2 wt.%) led to structural failure. This was primarily attributed to inefficient crosslinking caused by light absorption by the nanofiller, as well as increased thermal conductivity, which amplified the impact of the thermal treatment used to evaluate the nanostructure stability. It is also worth noting that formulations containing 2 wt.% of GO showed already a collapsed structure after UV irradiation (as described above). Finally, UV dose showed negligible influence within the tested range.

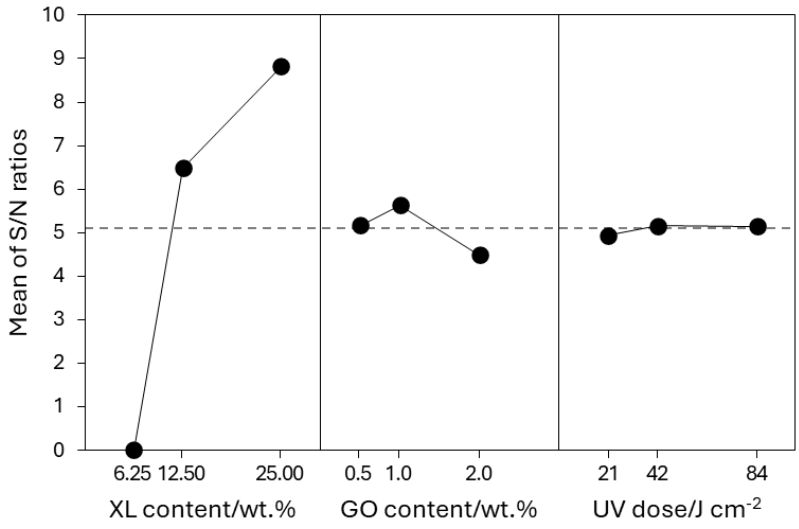

Fig. 6 *S/N* ratio plots for solvent and thermal shape stability as response parameter

To validate the stability results, FESEM (Field Emission Scanning Electron Microscopy) imaging was performed on mats rated as 1 (shape-stable) or 0 (partially shape-stable) for thermal resistance (Figure 7). FESEM analysis offers higher accuracy not only due to its superior resolution, but also because it allows examination of areas with a much greater fiber density, unlike optical microscopy, which is limited to zones with sparse or individual fibers. Electron microscopy confirmed that fibers in samples #6 and #9 remained intact after thermal treatment, while others exhibited partial collapse or fusion among fibers.

To evaluate the impact of GO content on shape stability, the results were compared with those from the neat system without GO [16,17]. As shown in Figure 7, sample #8 (12.5 wt.% XL, 0.5 wt.% GO) partially preserved its fibrous morphology: fibers were still visible, although some areas showed degradation or collapse. In contrast, a comparable sample without GO completely lost its fibrous structure after solvent or heat treatment (data not shown). Similarly, sample #9 (25 wt.% XL, 1 wt.% GO) demonstrated excellent fiber retention, significantly better than that of equivalent mats without GO. These findings suggest that the incorporation of GO positively influences the shape stability of electrospun photocured membranes, provided its content remains below 2 wt.%.

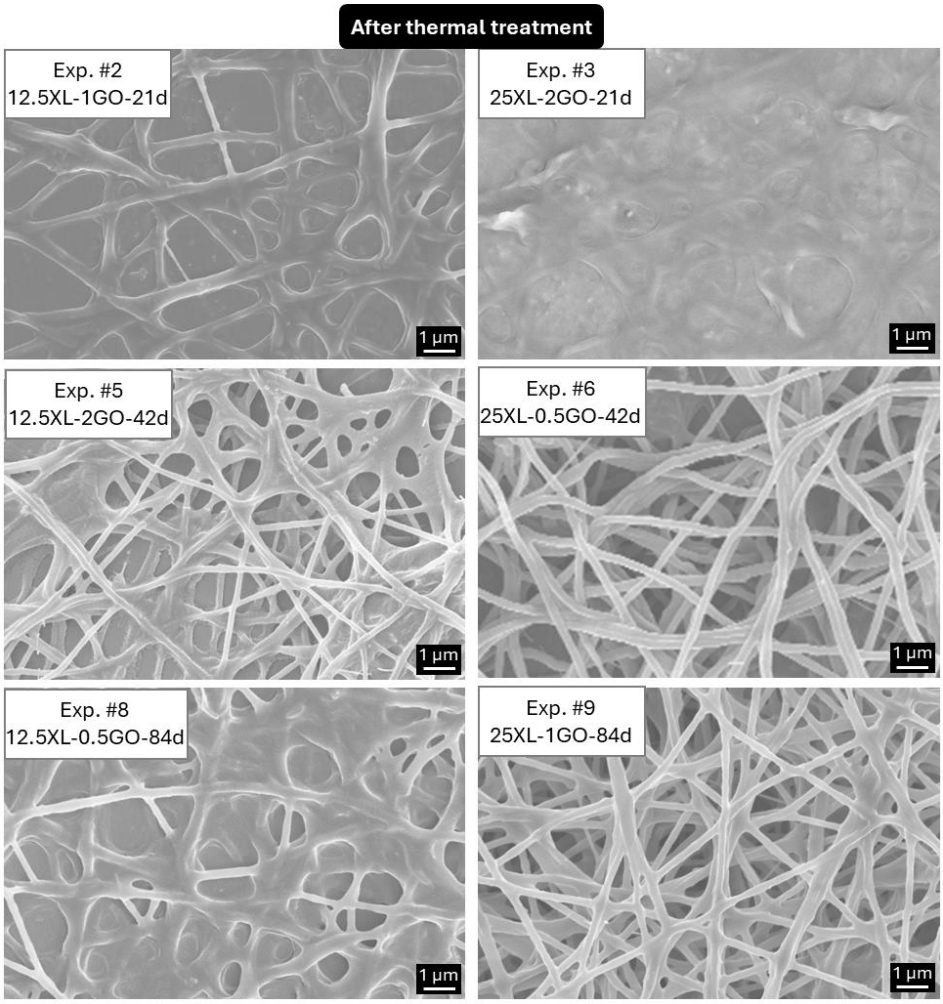

Fig. 7 FESEM images of the mats after thermal treatment (100 °C for 30 min)

From the analysis of the shape stability response, it can be concluded that to produce fully shape-stable PEO-based nanocomposite fibers with effective solvent and thermal resistance, the crosslinker content should be higher than 6.25 wt.%, while the GO content should be lower than 2 wt.%. The applied UV dose is instead almost irrelevant in the investigated range,

and a crosslinking conversion of around 45% is achieved, as estimated by FTIR-ATR on both sides of the membranes [17].

The optimized formulation (25 wt.% XL, 1 wt.% GO, dose of 84 J/cm² to maximize both the fibrous morphology stability and the photo-induced reduction of GO) was selected for thermal conductivity measurements. As shown in Figure 8, thermal diffusivity is nearly constant in a large temperature window and does not change even when the temperature overcomes the melting point of the crosslinked PEO (approximately 64°C) [17], confirming both the robustness and functional enhancement of the nanocomposite system. In fact, the obtained values are higher than those for neat PEO (with a thermal diffusivity of 0.21 mm^2/s for the electrospun nanocomposite mat compared to 0.15 mm^2/s for the PEO film).

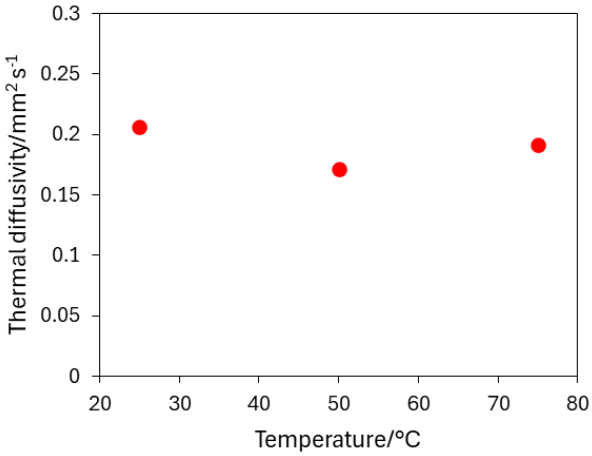

Fig. 8 Thermal diffusivity of optimized electrospun photocured mat (25XL-1GO-84d) as a function of temperature

The measured thermal diffusivity values of the nanocomposite mat are comparable to those of the corresponding continuous films (Figure 3). This observation highlights the complexity of thermal diffusivity, which is influenced by multiple interrelated factors. As a property, thermal diffusivity is directly proportional to thermal conductivity and inversely proportional to density. In fibrous mats, porosity lowers the bulk density and disrupts heat flow pathways, typically resulting in reduced thermal diffusivity. However, thermal conductivity in polymers is also strongly affected by structural features, which are in turn determined by processing conditions. For instance, electrospinning can enhance chain alignment and crystallinity, potentially leading to improved thermal diffusivity. In nanocomposite systems, additional factors come into play. Beyond the intrinsic properties and content of the filler, thermal diffusivity is influenced by the spatial distribution of the filler and the quality of interfacial bonding between the filler and the polymer matrix. Interfacial thermal resistance, arising at the contact surfaces between GO and the polymer, may differ significantly between fibrous and continuous morphologies, thereby affecting thermal transport behavior. Given that a comprehensive and predictive theory for thermal transport in bulk polymers is still lacking [47,48], predicting thermal conductivity in nanofibrous composite systems becomes even more

challenging due to the simultaneous influence of numerous structural and interfacial parameters.

Conclusions

In this work, we prepared novel nanofibrous nanocomposites based on PEO and incorporating GO and designed a light-assisted fabrication process to simultaneously crosslink the electrospun polymeric fibers and reduce GO to enhance shape stability and thermal conductivity. After electrospinning, irradiation of the fiber mat enabled the concurrent crosslinking of the polymer network and *in situ* reduction of GO within the fibrous matrix. The fabrication of nanofibrous membranes was successfully optimized using a Taguchi DoE, which identified crosslinker content as the primary factor influencing shape stability. Morphological analysis confirmed that, with an optimized combination of crosslinker and photoinitiator content, as well as appropriate UV exposure, the fiber integrity was maintained after both thermal and solvent treatments. The reduction of GO occurred concurrently with the photocrosslinking process, and the resulting presence of reduced GO enhanced the thermal diffusivity of the membranes across the tested temperature range.

Overall, this study presents a simple, scalable, and effective strategy for fabricating shape-stable, thermally conductive electrospun membranes

via photo-induced crosslinking and GO reduction. These multifunctional nanocomposites offer strong potential for applications in thermal management, wearable electronics, and advanced filtration systems.

Experimental

Materials

High molecular weight polyethylene oxide (PEO, *MW* 1,000,000 g/mol), benzophenone (≥ 99%), and trimethylolpropane trimethacrylate (TMPTMA) were purchased from Sigma-Aldrich. Graphene oxide water dispersion (0.4 wt.% concentration) was obtained from Graphenea. All other chemicals were purchased from Sigma-Aldrich.

Solution preparation

The electrospinning solutions, as well as the solution for film casting, were prepared by diluting the GO dispersion in distilled water and sonicating for 1 hour. Then PEO was added to the diluted GO dispersion to form a 5 wt.% aqueous solution of PEO with varying amounts of GO, which was magnetically stirred overnight at room temperature. Subsequently, the TMPTMA crosslinker (XL, in different concentrations) and the benzophenone PI (2 wt.% with respect to PEO) were added to PEO/GO formulations, and the solution was magnetically stirred for 15 minutes at room temperature.

Films preparation

To obtain continuous films, the solutions were cast onto a glass Petri dish and water was left to evaporate for 48 h. Films with a thickness between 50 and 300 μm were fabricated; the thickness was measured by digital micrometer.

Electrospun membranes preparation

Electrospinning was performed by an E-fiber electrospinning system SKE apparatus in horizontal setup with high-voltage power supply, a programmable syringe pump (syringe tip diameter of 1 mm) and a stationary collector. Aluminum foils were used as the substrate during electrospinning. The electrospun mats were prepared at ambient conditions (temperature of 20–23 °C and relative humidity of 45–50%) by applying a voltage of 14–16 kV and a flow rate of 0.1–0.2 ml/h, while the working distance was 15 cm. Membranes with a thickness of around 50–100 μm were fabricated. The thickness was measured by digital micrometer; for each sample at least 5 values in different spots of the membrane were collected and the average value was calculated.

Photocrosslinking

Photo-curing was performed by a Dymax ECE 5000 UV-Curing flood lamp with a light intensity of 70 mW/cm^2 in inert atmosphere (i.e., by purging N_2 in the curing chamber) for an irradiation time of 5, 10 or 20 minutes, thus

varying the UV light dose. The UV light intensity was measured by an EIT radiometer.

Design of Experiment (DoE)

In order to efficiently optimize the electrospinning formulations based on the performance of the obtained nanofibrous membranes, a DoE was conducted. A Taguchi design (orthogonal array) was implemented by Minitab software. Three processing variables (i.e., TMPTMA crosslinker content, GO content and UV dose) were chosen as factors for the analysis and three levels for each variable were considered (as detailed in Table 3). An L9 orthogonal array was obtained, and the 9 selected statistical experiments were performed. The signal-to-noise ratio (*S/N* ratio) for experiment was computed and the level of a desired signal to the level of background noise could be determined accordingly.

Table 3 Selected factors and levels used for the Taguchi DoE method

Factor	Level 1	Level 2	Level 3
XL content	6.25 wt.% (6.25XL)	12.50 wt.% (12.5XL)	25.00 wt.% (25XL)
GO content	0.5 wt.% (0.5GO)	1.0 wt.% (1GO)	2.0 wt.% (2GO)

UV dose	21 J/cm^2 (21d)	42 J/cm^2 (42d)	84 J/cm^2 (84d)

Characterization

UV-Vis spectroscopy was performed by means of a Evolution One Plus spectrophotometer (Thermo Fisher Scientific). The GO dispersion was diluted with water to reach a concentration of 0.0018 wt.%. The photoinitiator was added to the dispersion in a GO:photoinitiator weight ratio of 1:2. The solution was then irradiated with a UV dose of 84 J/cm^2. Spectra were acquired with a 1 nm resolution in the range 190–800 nm.

FTIR-ATR was performed on nanocomposite films and membranes with a Thermo Fisher Scientific Nicolet iS50 spectrophotometer. The crosslinking conversion was assessed at multiple locations across the sample surface, as well as on both the top and bottom sides of the samples.

XRD characterization was performed using a Panalytical X'Pert PRO (Cu Kα radiation) diffractometer, with a PIXcel detector, a solid-state detector with rapid readout time and high dynamic range. Data collection has been performed at 40 kV and 40 mA, between 5° and 50° *2θ*, with a step of 0.02° *2θ* and a wavelength of 1.54187 Å. PEO/XL/GO cast films were analyzed before and after irradiation with a UV dose of 42 J/cm^2.

The thermal diffusivity of the films and of the electrospun mats was measured by means of a Netzsch LFA 467 HyperFlash Light Flash Analyzer at 25 °C, 50 °C, and 75 °C in an inert N_2 atmosphere. PEO/XL/GO cast films were analyzed before and after irradiation with a UV dose of 42 J/cm^2. Tested films had a thickness of 300 μm; in the case of electrospun samples, multiple mats were overlapped to form a thick sample of around 300 μm. Tests were performed employing a laser voltage of 250 V and a pulse width of 30 μs, with five repeated measurements per specimen. The Proteus® software (NETZSCH, version 8.0.3) was used for data analysis.

The electrospun fiber morphology was monitored by means of an Olympus BX53M optical microscope and by a ZEISS Supra 40 FESEM. The samples were coated with a 10-nm Cr film via sputtering (by a Quorum Q150T ES sputter coater) prior to electron microscopy analysis. The distribution of fiber diameters was obtained analyzing the FESEM images by ImageJ software: approximately 100 measurements were taken for each sample.

Compliance with Ethical Standards

The authors declare that they have no conflict of interests that are directly or indirectly related to the work presented in this article.

References

1. Ji D, Lin Y, Guo X, Ramasubramanian B, Wang R, Radacsi N, Jose R, Qin X, Ramakrishna S (2024) Nat. Rev. Methods Primer 4:1. DOI: 10.1038/s43586-023-00278-z
2. Keirouz A, Wang Z, Reddy V S, Nagy Z K, Vass P, Buzgo M, Ramakrishna S, Radacsi N (2023) Adv. Mater. Technol. 8:2201723. DOI: 10.1002/admt.202201723
3. Li Y, Zhu J, Cheng H, Li G, Cho H, Jiang M, Gao Q, Zhang X (2021). Adv. Mater. Technol. 6:2100410. DOI: 10.1002/admt.202100410
4. Bachs-Herrera A, Yousefzade O, del Valle L J, Puiggali J (2021) Appl. Sci. 11:1808. DOI: 10.3390/app11041808
5. Avossa J, Herwig G, Toncelli C, Itel F, Rossi R M (2022) Green Chem. 24:2347. DOI: 10.1039/D1GC04252A
6. Ma S, Li A, Pan L (2024) Polymers 16:2459. DOI: 10.3390/polym16172459
7. González E, Barquero A, Paulis M, Leiza J R (2023) Macromol. Mater. Eng. 308:2300011. DOI: 10.1002/mame.202300011
8. Kausar A, Ahmad I (2023) J. Compos. Sci. 7:290. DOI: 10.3390/jcs7070290
9. Zhang M, Song W, Tang Y, Xu X, Huang Y, Yu D (2022) Polymers 14:351. DOI: 10.3390/polym14020351
10. Shetty K, Bhandari A, Yadav K S (2022) J. Controlled Release 350:421. DOI: 10.1016/j.jconrel.2022.08.035
11. Afsari N, Eslahi N, Varsei M, Ghanbari H (2023) J. Appl. Polym. Sci. 140:e54015. DOI: 10.1002/app.54015
12. Ahmadijokani F, Molavi H, Bahi A, Fernández R, Alaee P, Wu S, Wuttke S, Ko F, Arjmand M (2022) Adv. Funct. Mater. 32:2207723. DOI: 10.1002/adfm.202207723
13. Zhang J, Yu M, Tao S (2024) Nano Res. 17:7077. DOI: 10.1007/s12274-024-6753-8
14. Kianfar P, Dalle Vacche S, Bongiovanni R, Mollea C, Bosco F, Najmi Z, Scalia A C, Cochis A, Vitale A (2024) ACS Appl. Polym. Mater. 6:14749. DOI: 10.1021/acsapm.4c02953
15. Kianfar P, Bakry A, Dalle Vacche S, Bongiovanni R, Vitale A (2024) J. Mater. Sci. 59:3711. DOI: 10.1007/s10853-024-09416-8
16. Kianfar P, Vitale A, Dalle Vacche S, Bongiovanni, R (2021) J. Mater. Sci., 56 (2), 1879. DOI: 10.1007/s10853-020-05346-3.
17. Fredi, G, Kianfar, P, Dalle Vacche S, Pegoretti A, Vitale A (2021) Polymers 13:2979. DOI: 10.3390/polym13172979

18. Kianfar P, Vitale A, Dalle Vacche S, Bongiovanni R (2019) Carbohydr. Polym. 217:144. DOI: 10.1016/j.carbpol.2019.04.062
19. Razaq A, Bibi F, Zheng X, Papadakis R, Jafri S H M, Li H (2022) Materials 15:1012. DOI: 10.3390/ma15031012
20. Papageorgiou D G, Kinloch I A, Young R J (2017) Prog. Mater. Sci. 90:75. DOI: 10.1016/j.pmatsci.2017.07.004
21. Wu J, Lin H, Moss D J, Loh K P, Jia B (2023) Nat. Rev. Chem. 7:162. DOI: 10.1038/s41570-022-00458-7
22. Soni J, Teli P, Agarwal S (2024) Curr. Nanosci. 20:146. DOI: 10.2174/1573413719666230329104621
23. Agarwal V, Zetterlund P B (2021) Chem. Eng. J. 405:127018. DOI: 10.1016/j.cej.2020.127018
24. Toh S Y, Loh K S, Kamarudin S K, Daud W R W (2014) Chem. Eng. J. 251:422. DOI: 10.1016/j.cej.2014.04.004
25. Plotnikov V G, Smirnov V A, Alfimov M V, Shul'ga Y M (2011) High Energy Chem. 45:411. DOI: 10.1134/S0018143911050158
26. Xue B, Zou Y, Yang Y (2017) J. Mater. Sci. 52:4866. DOI: 10.1007/s10853-016-0721-y
27. Mangadlao J D, Cao P, Choi D, Advincula R C (2017) ACS Appl. Mater. Interfaces 9:24887. DOI: 10.1021/acsami.7b06275
28. Acosta Ortiz R, García Valdez A E, Ku Herrera J de J (2020) Polym.-Plast. Technol. Mater. 59:282. DOI: 10.1080/25740881.2019.1634726
29. Gigot A, Morra A, Castellino M, Pirri C F, Mittal V, Dietliker K, Sangermano M (2017) Polymer 108:251. DOI: 10.1016/j.polymer.2016.11.064
30. Sharif M, Pourabas B, Fazli A (2016) J. Photopolym. Sci. Technol. 29:769. DOI: 10.2494/photopolymer.29.769
31. Fabbri P, Valentini L, Bittolo Bon S, Foix D, Pasquali L, Montecchi M, Sangermano M (2012) Polymer 53:6039. DOI: 10.1016/j.polymer.2012.10.045
32. Ghorbanzadeh Sheish S, Emadi R, Ahmadian M, Sadeghzade S, Tavangarian F (2021) Polymers 13:913. DOI: 10.3390/polym13060913
33. Barkhordari S, Hamzehlouy A, Tavakoli Dare M, Jafari A, Dehchani A J, Dawi E A, Ahmadi T, Khonakdar H A (2024) Polym.-Plast. Technol. Mater. 63:2563. DOI: 10.1080/25740881.2024.2378096
34. Narayanan K B, Park G T, Han S S (2020) Colloids Surf. B Biointerfaces 191:110994. DOI: 10.1016/j.colsurfb.2020.110994
35. Magaz A, Li X, Gough J E, Blaker J J (2021) Mater. Sci. Eng. C 119:111632. DOI: 10.1016/j.msec.2020.111632
36. Altinbasak I, Jijie R, Barras A, Golba B, Sanyal R, Bouckaert J, Drider D, Bilyy R, Dumych T, Paryzhak S, Vovk V, Boukherroub R, Sanyal

A, Szunerits S (2018) ACS Appl. Mater. Interfaces 10:41098. DOI: 10.1021/acsami.8b14784
37. Su Y, Zhang W, Lan J, Sui G, Zhang H, Yang X (2020) ACS Appl. Nano Mater. 3:7005. DOI: 10.1021/acsanm.0c01328
38. Shahitha Parveen J, Thirumurugan M, Dhakshnamoorthy M, Sathik Basha S, Daulath Banu R, Hari Shankar V (2024) Mater. Lett. 355:135545. DOI: 10.1016/j.matlet.2023.135545
39. Kenawy E-R, Azaam M M, Eldeep A Z, Ramzy G H, Ali A I, Youssry S M (2025) J. Inorg. Organomet. Polym. Mater. 35:2643. DOI: 10.1007/s10904-024-03402-y
40. Chen J-X, Li J-W, Jiang Z-J, Chiu C-W (2024) Chem. Eng. J. 498:155244. DOI: 10.1016/j.cej.2024.155244
41. Mobasheri A, Parhoodeh S, Shams G (2022) Fibers Polym. 23:784. DOI: 10.1007/s12221-022-3718-y
42. Kausar A, Ahmad I, Lam T D (2024) Pure Appl. Chem. 96:1043. DOI: 10.1515/pac-2023-0803
43. Köroğlu D, Eskitoros-Togay Ş M, Dilsiz N (2024) J. Appl. Polym. Sci. 141:e55995. DOI: 10.1002/app.55995
44. Ragab H M (2022) J. Mater. Sci. Mater. Electron. 33:19793. DOI: 10.1007/s10854-022-08789-3
45. Wen J, Zhao Q, Jiang X, Ji G, Wang R, Lu G, Long J, Hu N, Xu C (2021) ACS Appl. Energy Mater. 4:3660. DOI: 10.1021/acsaem.1c00090
46. Stobinski L, Lesiak B, Malolepszy A, Mazurkiewicz M, Mierzwa B, Zemek J, Jiricek P, Bieloshapka I (2014) J. Electron Spectrosc. Relat. Phenom. 195:145. DOI: 10.1016/j.elspec.2014.07.003
47. Xu X F, Chen J, Zhou J, Li B W (2018) Adv. Mater. 30:1705544. DOI: 10.1002/adma.201705544
48. Li Z, Sun Y, Hu F, Liu D, Zhang X, Ren J, Guo H, Shalash M, He M, Hou H, El-Bahy S M (2025) J. Mater. Sci. & Technol. 218:191. DOI: 10.1016/j.jmst.2024.07.053

Figure Captions

Fig. 1 Schematic illustration of the photo-induced fabrication of crosslinked PEO-based electrospun nanofibers incorporating *in situ* reduced GO

Fig. 2 UV-Vis spectra and photographs of GO water dispersion in the presence of the photoinitiator, before and after irradiation

Fig. 3 XRD patterns of GO, PEO powder and PEO/XL/GO cast films with 1 (a) and 5 wt.% (b) GO, before and after UV irradiation

Fig. 4 Thermal diffusivity of PEO/XL/GO cast films with 0 and 1 wt.% GO, before and after UV irradiation (with a UV dose of 42 J/cm^2)

Fig. 5 Morphology of the nanocomposite PEO-based electrospun mats: FESEM images and fiber diameter distribution

Fig. 6 S/N ratio plots for solvent and thermal shape stability as response parameter

Fig. 7 FESEM images of the mats after thermal treatment (100 °C for 30 min)

Fig. 8 Thermal diffusivity of optimized electrospun photocured mat (25XL-1GO-84d) as a function of temperature

Table 1. Taguchi L9 experimental orthogonal array design for electrospun nanocomposites

Exp. #	XL/wt.%	GO/wt.%	d/J cm^{-2}
1	6.25	0.5	21
2	12.5	1	21
3	25	2	21
4	6.25	1	42
5	12.5	2	42
6	25	0.5	42
7	6.25	2	84
8	12.5	0.5	84
9	25	1	84

Table 2. Shape stability results from solvent and thermal treatments of the L9 experiments: 1 = shape-stable, 0 = partially shape-stable, -1 = shape unstable

Exp. #	Shape stability response	
	Solvent resistance	Thermal resistance
1	-1	-1
2	1	0
3	1	0
4	-1	-1
5	0	0
6	1	1
7	-1	-1
8	0	0
9	1	1

Table 3 Selected factors and levels used for the Taguchi DoE method

Factor	Level 1	Level 2	Level 3
XL content	6.25 wt.% (6.25XL)	12.50 wt.% (12.5XL)	25.00 wt.% (25XL)
GO content	0.5 wt.% (0.5GO)	1.0 wt.% (1GO)	2.0 wt.% (2GO)
UV dose	21 J/cm^2 (21d)	42 J/cm^2 (42d)	84 J/cm^2 (84d)

Figure 1

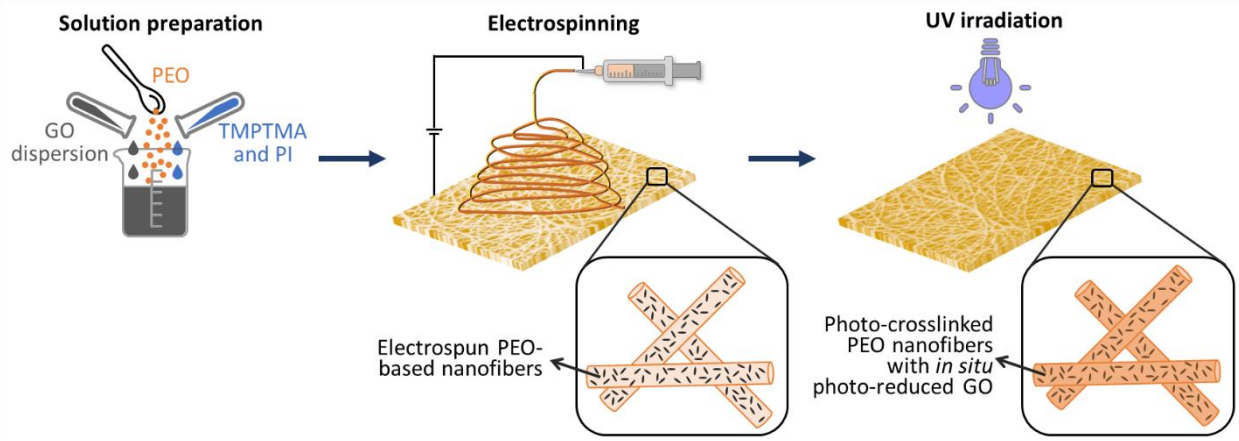

Figure 2

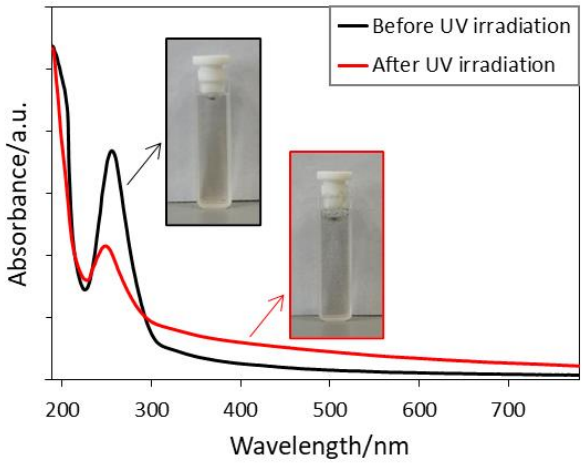

Figure 3

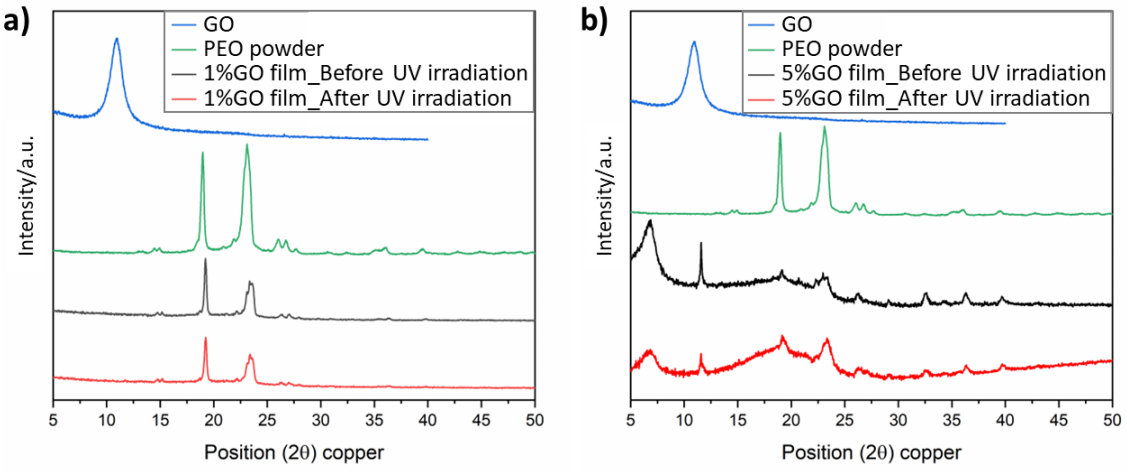

Figure 4

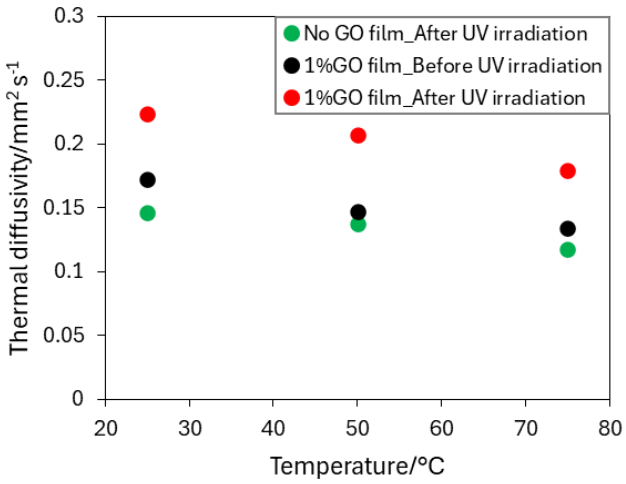

Figure 5

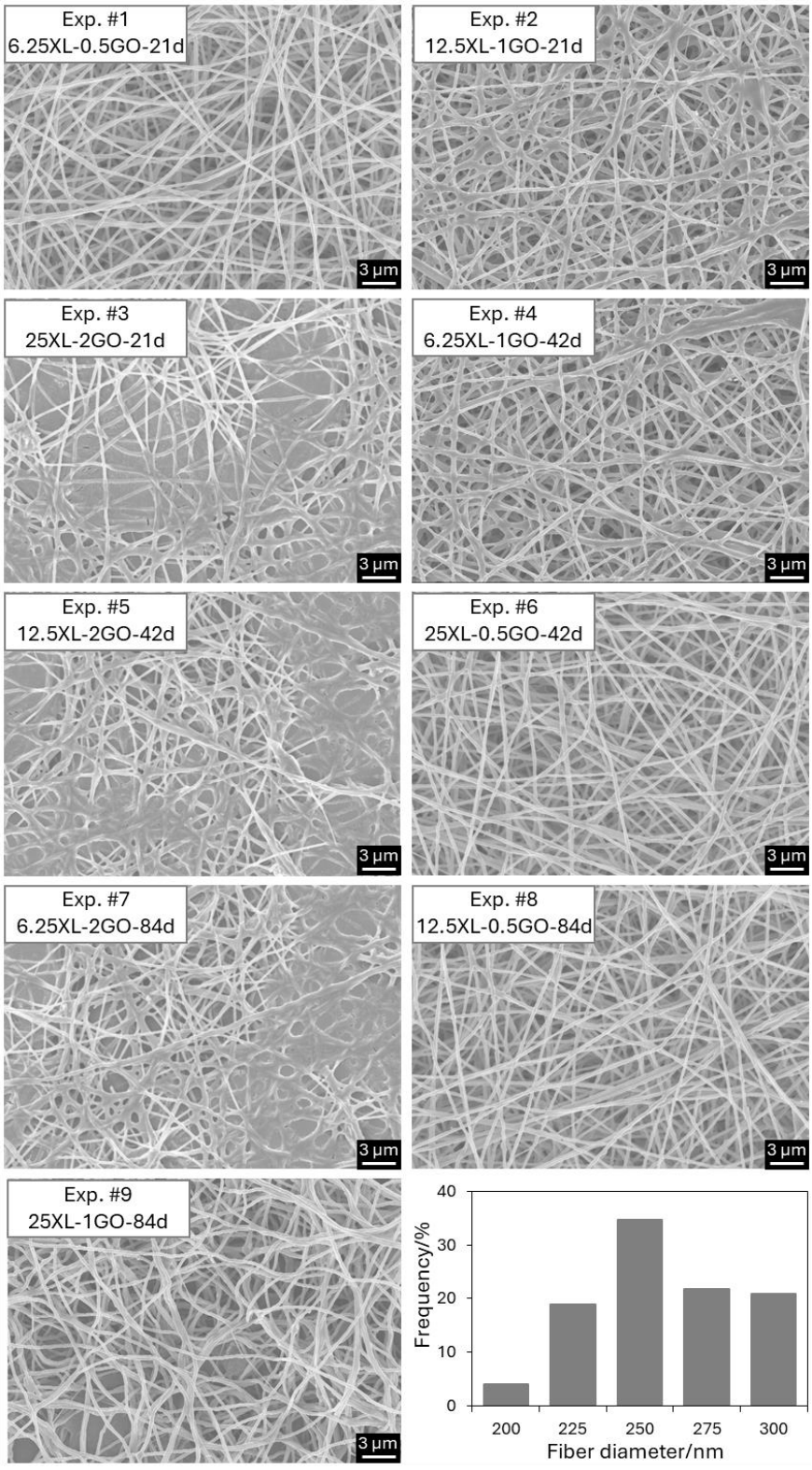
Exp. #1
6.25XL-0.5GO-21d
Exp. #2
12.5XL-1GO-21d
Exp. #3
25XL-2GO-21d
Exp. #4
6.25XL-1GO-42d
Exp. #5
12.5XL-2GO-42d
Exp. #6
25XL-0.5GO-42d
Exp. #7
6.25XL-2GO-84d
Exp. #8
12.5XL-0.5GO-84d
Exp. #9
25XL-1GO-84d
3 μm
Frequency/%
0
10
20
30
40
200
225
250
275
300
Fiber diameter/nm

Figure 6

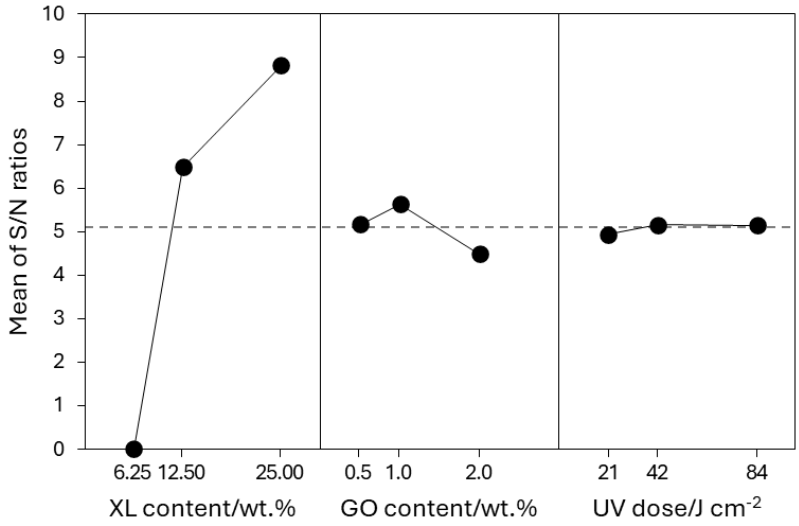

Figure 7

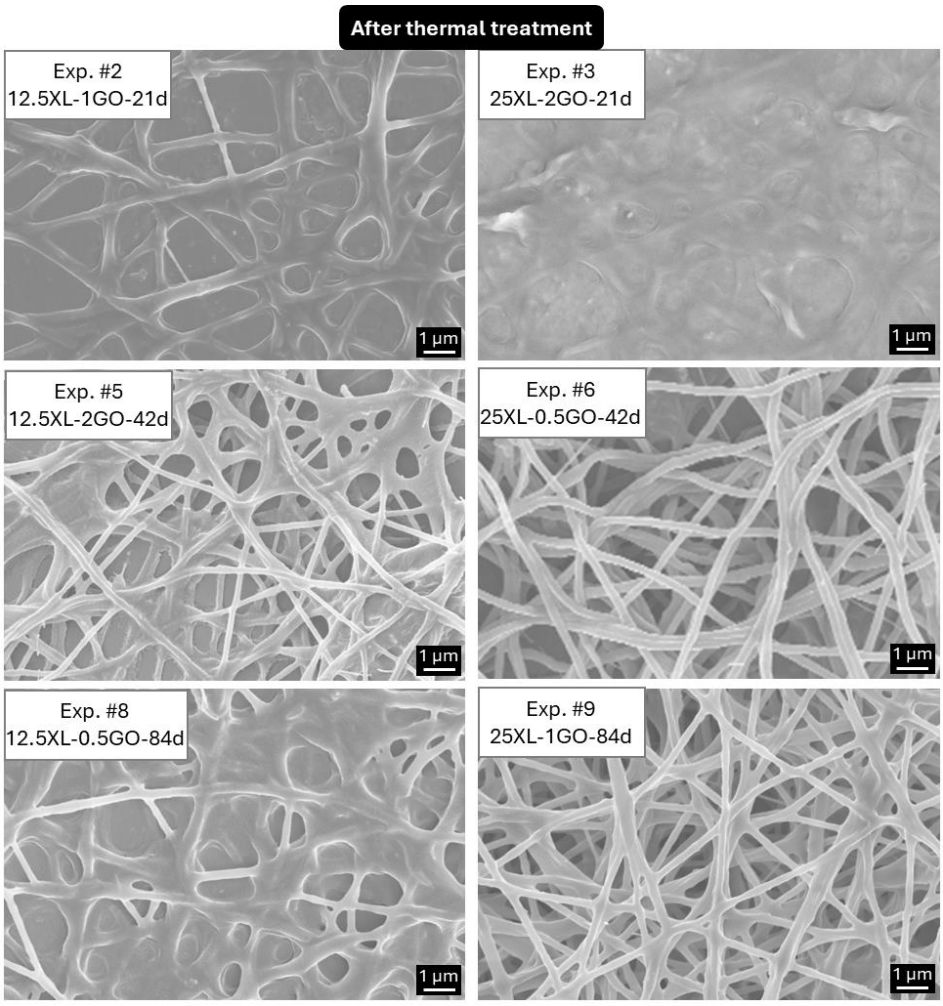

Figure 8

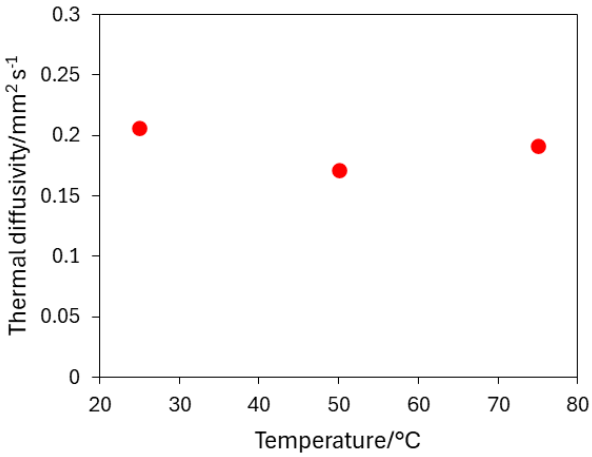
0.3
0.25
0.2
0.15
0.1
0.05
0
Thermal diffusivity/mm^2 s^{-1}
20
30
40
50
60
70
80
Temperature/°C